

# Predicting Accurate X-ray Absorption Spectra for $\text{CN}^+$ , $\text{CN}^\bullet$ , and $\text{CN}^-$ : Insights from First-Principles Simulations

JINYU LI,<sup>1</sup> SHENG-YU WANG,<sup>1</sup> LU ZHANG,<sup>1</sup> GUOYAN GE,<sup>1</sup> MINRUI WEI,<sup>1</sup> JUNXIANG ZUO,<sup>1</sup> AND WEIJIE HUA<sup>1</sup>

<sup>1</sup>MIT Key Laboratory of Semiconductor Microstructure and Quantum Sensing, Department of Applied Physics, School of Physics, Nanjing University of Science and Technology, 210094 Nanjing, China

## ABSTRACT

High-resolution X-ray spectroscopy is an essential tool in X-ray astronomy, enabling detailed studies of celestial objects and their physical and chemical properties. However, comprehensive mapping of high-resolution X-ray spectra for even simple interstellar and circumstellar molecules is still lacking. In this study, we conducted systematic quantum chemical simulations to predict the C1s X-ray absorption spectra of  $\text{CN}^+$ ,  $\text{CN}$ , and  $\text{CN}^-$ . Our findings provide valuable references for both X-ray astronomy and laboratory studies. We assigned the first electronic peak of  $\text{CN}^+$  and  $\text{CN}$  to  $\text{C1s} \rightarrow \sigma^*$  transitions, while the peak for  $\text{CN}^-$  corresponds to a  $\text{C1s} \rightarrow \pi^*$  transition. We further calculated the vibronic fine structures for these transitions using the quantum wavepacket method based on multiconfigurational-level, anharmonic potential energy curves, revealing distinct energy positions for the 0-0 absorptions at 280.7 eV, 279.6 eV, and 285.8 eV. Each vibronic profile features a prominent 0-0 peak, showing overall similarity but differing intensity ratios of the 0-0 and 0-1 peaks. Notably, introducing a C1s core hole leads to shortened C-N bond lengths and increased vibrational frequencies across all species. These findings enhance our understanding of the electronic structures and X-ray spectra of carbon-nitrogen species, emphasizing the influence of charge state on X-ray absorptions.

*Keywords:* X-ray astronomy; interstellar and circumstellar molecules; X-ray absorption spectroscopy; vibronic fine structure; quantum wavepacket method;

## 1. INTRODUCTION

X-ray astronomy, the study of X-ray radiation emitted by celestial bodies, has played a crucial role in unraveling the mysteries of the dynamic universe at all scales, from planets to distant galaxies and star clusters (Giacconi 2003; Arnaud et al. 2011; Beckman 2021; Gandhi 2024). With a rich history spanning over 60 years, X-ray observations have led to the discovery of a diverse range of cosmic X-ray sources, beginning with the first detection of an X-ray source outside the Sun in 1962 (Giacconi et al. 1962) and culminating in the cataloging of over 60,000 discrete sources by the ROSAT observatory (Trümper 1993). The field then evolved

from simple observations of X-ray sources to comprehensive studies of X-ray spectroscopy (Bambi & Jiang 2023; Wilkes et al. 2022; Ezoe et al. 2021; Kahn 1999; Oda 1986; Longair 1994; Mannings et al. 2000; Kaastra et al. 2008), offering valuable insights into the physical conditions of astrophysical plasmas. Although cosmic X-ray sources are often faint, X-ray spectral observations are essential across many sub-disciplines of astrophysics, as they provide critical information (temperature, density, velocity, gravity, etc.) of emitting plasmas—data that cannot be obtained through ground-based experiments. The visibility of discrete spectral features in astrophysical X-ray spectra is primarily influenced by three factors: photoelectric absorption in the interstellar medium, reduced high-energy sensitivity due to focusing optics, and the cosmic abundance of elements. High-resolution X-ray spectroscopy has emerged as a powerful tool for investigating a wide variety of astrophysical plasmas, yielding critical information about physical phenomena occurring in extreme environments character-

wangshengyu@njust.edu.cn

jxzuo@njust.edu.cn

wjhua@njust.edu.cn

ized by strong gravity, intense magnetic fields, and rapid gas motion (Bambi & Jiang 2023; Ezoe et al. 2021). The unique insights gained through X-ray spectroscopy are vital for advancing our understanding of the dynamic universe.

CN,  $\text{CN}^+$ , and  $\text{CN}^-$  are important interstellar molecules or ions. The CN ( $X^2\Sigma^+$ ) radical was the second molecule, after methylidyne (CH), detected in space (McKellar 1940). In 1995, Bakker et al (Bakker et al. 1995). discovered CN and  $\text{C}_2$  absorption lines in secondary stars. CN is particularly noteworthy as its millimeter-wave line emission is widely employed as a probe of dense molecular gas and photon-dominated regions of the galactic interstellar medium (ISM) (Boger & Sternberg 2005). Observations of characteristic absorption lines of CN in interstellar dust and gas, including those from molecular interfaces in star-forming regions, can reveal the abundance and distribution of chemical elements in interstellar space. The positively charged cyanogen ion,  $\text{CN}^+$ , was discovered in comets at 2181 and 3185 Å through ultraviolet transitions by Snyder et al. in 1992 (Snyder 1992). The Goddard High Resolution Spectrograph (GHRS) on the Hubble Space Telescope also detected absorption lines of  $\text{CN}^+$  in the interstellar environment (Savage & Sembach 1996). Given the prevalence of CN radicals in space,  $\text{CN}^+$  is a promising candidate for future radio astronomy searches. This cation plays a significant role in interstellar chemical processes, with its distribution in interstellar space closely linked to the physical conditions and chemical composition of interstellar dust clouds. The possible relevance of the corresponding anion,  $\text{CN}^-$ , to astrochemistry, has been considered since the 1970s (Dalgarno & McCray 1973; Sarre 1980), with laboratory observations of rotational spectroscopy finally achieved in 2000 (Gottlieb et al. 2007; Amano 2008). The cyanide anion,  $\text{CN}^-$ , is the first diatomic anion detected by astronomy and has garnered significant attention from scientists due to its unique existence and mechanisms in interstellar space (Agúndez et al. 2010). Currently, the molecular anions detected in interstellar and circumstellar gases are predominantly heavier linear carbon chains composed of three or more carbon atoms. Therefore, studying the abundance of these astronomical anions should first focus on shorter anions, particularly  $\text{CN}^-$ , which form very slowly via radiative electron attachment.

In the laboratory, the three systems—CN,  $\text{CN}^+$ , and  $\text{CN}^-$ —have been extensively studied both experimentally and theoretically in the fields of atomic, molecular, and optical (AMO) physics and physical chemistry, providing important references for identify-

ing and understanding these interstellar molecules or ions. For instance, CN has been the focus of numerous laboratory spectroscopic studies in the optical/ultraviolet, infrared, and millimeter-wave regions for decades (Brooke et al. 2014; Yin et al. 2018). In the X-ray regime, recent studies have concentrated on obtaining high-resolution X-ray absorption (XAS) or photoelectron (XPS) spectra of diatomic molecules ( $\text{N}_2$ , CO, and NO), cations ( $\text{NH}^+$ ,  $\text{N}_2^+$ ,  $\text{CO}^+$ , and  $\text{NO}^+$ ), and anions ( $\text{C}_2^-$ ) (Carniato et al. 2020; Schippers et al. 2023; Ehara et al. 2006; Püttner et al. 1999; Lindblad et al. 2020; Couto et al. 2020; Lindblad et al. 2022). Vibronic coupling is a significant source of fine structure. Recent studies utilizing density functional theory (DFT) and multiconfigurational methods have demonstrated accurate vibrationally-resolved XPS/XAS spectra for various molecules ( $\text{N}_2$ , CO, and NO) and cations ( $\text{N}_2^+$ ,  $\text{CO}^+$ , and  $\text{NO}^+$ ) at the C/N/O K-edges, which align well with available high-resolution experimental data. Notably, diatomic systems exhibit greater sensitivity to anharmonic effects compared to polyatomic systems (Zhang et al. 2024). To our knowledge, no experimental spectra are currently available for comparison for the three carbon-nitrogen species.

The necessity of studying  $\text{CN}^+$ , CN, and  $\text{CN}^-$  also stems from the fact that the CN group serves as a crucial building block for larger interstellar or circumstellar molecules/ions, such as HCN (Snyder & Buhl 1971), HNC (Schilke et al. 2003), CCN (Anderson & Ziurys 2014), FeCN (Zack et al. 2011), KCN (Ziurys 2006), MgCN (Ziurys 2006), MgNC (Ziurys 2006), NaCN (Ziurys 2006), SiCN (Guélin et al. 2000), SiNC (Guélin et al. 2004),  $\text{H}_2\text{CN}$  (Ohishi et al. 1994),  $\text{H}_2\text{CN}^+$  (Smith 1988), CNCN (Agúndez et al. 2018),  $\text{CH}_3\text{CN}$  (Remijan et al. 2005),  $\text{CH}_3\text{CN}$  (Remijan et al. 2005) and  $\text{C}_3\text{H}_7\text{CN}$  (Guélin et al. 2000). A thorough investigation of the three diatomic species will provide fundamental insights for future studies of more complex interstellar or circumstellar species.

This study aims to simulate high-resolution, vibrationally-resolved XAS spectra of CN,  $\text{CN}^+$ , and  $\text{CN}^-$  at the carbon K-edge, which will be useful for future identifications in astronomical, physical, and chemical studies. Additionally, it will help elucidate the influence of charge state, or valence-shell ionization, on the XAS spectrum. Besides the spectra, we will conduct a systematic investigation of the electronic structure of these species at both the ground (GS) and the C1s core-excited states, including energy level diagrams, molecular orbital (MO) analysis, and potential energy curves (PECs). Understanding their electronic structures is fundamental for interpreting their spec-

troscopic and various other properties.  $\text{CN}^+$ ,  $\text{CN}$ , and  $\text{CN}^-$  possess 13, 14, and 15 electrons, respectively, with  $\text{CN}^+$  and  $\text{CN}^-$  being closed-shell systems with a singlet ground state ( $S_0$ ), while  $\text{CN}$  is an open-shell system with a doublet ground state ( $D_0$ ). Our calculations will encompass DFT with the full core hole (FCH) approximation and multiconfigurational methods, including state-averaged restricted active space self-consistent field (SA-RASSCF) (Malmqvist et al. 1990; Delcey et al. 2015; Stålring et al. 2001) and multi-state second-order perturbation theory restricted active space (MS-RASPT2) (Finley et al. 1998; Granovsky 2011).

Technically, obtaining accurate absolute core-level transition energies poses a challenge in quantum chemistry. For multiconfigurational methods, the C/N/O K-edge excitations typically exhibit an accuracy of several eV (Hua 2024; Zhang et al. 2016). The DFT-based  $\Delta$ Kohn-Sham ( $\Delta$ KS) (Schmidt et al. 1993; Triguero et al. 1999; Bagus 1965) method generally achieves an accuracy of 0.5-1.0 eV for 1s excitations of light elements (Bagus et al. 2016; Takahashi & Pettersson 2004; Du et al. 2022). To facilitate our energy predictions, we have chosen  $\text{CO}^+$ , which has high-resolution experimental data (Couto et al. 2020) for comparison, as a reference system for calibration and comparison purposes.  $\text{CO}^+$  is an isoelectronic species to  $\text{CN}$ , making it interesting to study the influence of  $\text{N} \leftrightarrow \text{O}^+$  replacement. At each theoretical method, the shift  $\delta$  was first obtained for  $\text{CO}^+$ , and this shift is assumed to be transferable to the carbon-nitrogen species.

## 2. COMPUTATIONAL DETAILS

### 2.1. Ground-state electronic structure by DFT

$\text{CN}^+$ ,  $\text{CN}$ ,  $\text{CN}^-$ , and  $\text{CO}^+$  were oriented along the  $Z$  axis, with carbons aligned in the same direction. All geometries were relaxed by DFT with the BLYP functional (Lee et al. 1988; Becke 1988) via the GAMESS-US package (Schmidt et al. 1993; Gordon & Schmidt 2005). The IGLO-III basis set (Kutzelnigg et al. 1990) was set for carbon and aug-cc-pVTZ (Kendall et al. 1992; Dunning 1989) for nitrogen or oxygen, ensuring consistency with subsequent X-ray spectral calculations with DFT. An energy level diagram was generated at each optimized geometry, visualizing and assigning all occupied and low-lying virtual MOs.

### 2.2. (Electronic-only) XAS

At the optimized GS geometry of each system, the C1s XAS spectrum was simulated using DFT, RASSCF, and RASPT2. DFT calculations employed the full core hole approximation (Triguero et al. 1998). For multiconfigu-

rational calculations, state-averaged (SA) CASSCF over 5 valence states was first performed, with the active space denoted as  $\text{CAS}(N_{el}, o)$ , where  $N_{el}$  and  $o$  represent the number of active electrons and orbitals, respectively. Specifically, 12 active orbitals were used, with  $N_{el}$  set to 10/11/12 for  $\text{CN}^+/\text{CN}/\text{CO}^+/\text{CN}^-$ . While only the ground state is directly related to XAS, it is standard practice to include additional valence-excited states for state averaging. This was followed by SA-RASSCF calculations over 30 C1s excited states. Consistent active space was selected for each system:  $\text{CN}^+$ ,  $\text{RAS}(10, 1/11/0)$ ;  $\text{CN}$  and  $\text{CO}^+$ ,  $\text{RAS}(11, 1/11/0)$ ; and  $\text{CN}^-$ ,  $\text{RAS}(12, 1/11/0)$ . The notation  $\text{RAS}(N_{el}, o_1/o_2/o_3)$  followed previous studies (Hua et al. 2016b; Zhang et al. 2016; Hua et al. 2016a, 2019b), where  $o_1/o_2/o_3$  denotes sizes of the RAS1/RAS2/RAS3 spaces, respectively, with RAS1 fixed to the C1s orbital with one electron. These calculations were performed using the Molpro package (Werner et al. 2012), with the aug-cc-pVTZ basis set (Kendall et al. 1992; Dunning 1989) for both atoms. Oscillator strengths were then computed from the wavefunctions of the initial and final states using our MCNOX code (Hua et al. 2019a; Hua 2024). To validate results and assess dynamic correlation effects, additional multiconfigurational simulations were conducted with the openMOL-CAS software (Li Manni et al. 2023; Fdez. Galván et al. 2019; Aquilante et al. 2020), employing both the SA-RASSCF (Malmqvist et al. 1990; Delcey et al. 2015; Stålring et al. 2001) and MS-RASPT2 (Finley et al. 1998; Granovsky 2011) methods, with the same basis set. Oscillator strengths were computed via the RAS state-interaction (RASSI) approach (Malmqvist & Roos 1989; Malmqvist et al. 2002). Specifically for  $\text{CN}^-$ , the cc-pVDZ basis set (Kendall et al. 1992) was employed to capture a broader spectrum in the higher energy region, with all other parameters set the same (Fig. A1).

For each method, the theoretical spectrum of  $\text{CO}^+$  was uniformly shifted by  $\delta$  to align the first resolved peak to the experiment (Couto et al. 2020). This shift was then applied to calibrate the spectra of all other systems. A half-width at half-maximum (HWHM) value of 0.4eV was used for spectral broadening across all four systems.

### 2.3. Multiconfigurational PECs

Multiconfigurational PECs for  $\text{CN}^+/\text{CN}/\text{CN}^-$  were simulated at varying bond distances, ranging from 0.7 to 1.22 Å in increments of 0.04 Å, and from 1.22 to 2.42 Å in increments of 0.1 Å. At each snapshot, valence states were first simulated, with all parameters set the same as at the GS geometry. Then, vertical PECs were

generated with all parameters set the same as at the GS geometry, except that only the 5 lowest C1s core-excited states were simulated. Besides SA-RASSCF calculations with Molpro (Werner et al. 2012), for validation, the openMOLCAS software (Li Manni et al. 2023; Fdez. Galván et al. 2019; Aquilante et al. 2020) was also employed to simulate the PECs with both the SA-RASSCF (Malmqvist et al. 1990; Delcey et al. 2015; Stålring et al. 2001) and MS-RASPT2 (Finley et al. 1998; Granovsky 2011) methods. The aug-cc-pVTZ (Kendall et al. 1992; Dunning 1989) was always used.

Multiconfigurational PECs for  $\text{CN}^+/\text{CN}/\text{CN}^-$  were simulated at varying bond distances, ranging from 0.7 to 1.22 Å in increments of 0.04 Å, and from 1.22 to 2.42 Å in increments of 0.1 Å. At each snapshot, valence states were first simulated with all parameters set the same as the GS geometry. Subsequently, vertical PECs were generated, maintaining the same GS parameters but simulating only the 5 lowest C1s core-excited states. For validation, in addition to SA-RASSCF calculations with Molpro (Werner et al. 2012), the openMOLCAS software (Li Manni et al. 2023; Fdez. Galván et al. 2019; Aquilante et al. 2020) was utilized to simulate the PECs using both the SA-RASSCF (Malmqvist et al. 1990; Delcey et al. 2015; Stålring et al. 2001) and MS-RASPT2 (Finley et al. 1998; Granovsky 2011) methods. The aug-cc-pVTZ basis set (Kendall et al. 1992; Dunning 1989) was consistently employed throughout. Each PEC is fitted to the Morse potential (Morse 1929):

$$E(R) = T_e + D_e[1 - e^{-\alpha(R-R_e)}]^2. \quad (1)$$

Here,  $R_e$  denotes the equilibrium internuclear distance,  $D_e$  stands for the dissociation energy (well depth),  $\alpha = \sqrt{k_e/2D_e}$  represents a potential width parameter with  $k_e = \left[\frac{d^2U(R)}{dR^2}\right]_{R=R_e}$  being the force constant at  $R_e$ , and  $T_e$  is a constant term. Raw data of all PECs are provided in the Supplementary Material.

#### 2.4. *Vibrationally-resolved XAS*

The theory for computing vibrationally-resolved XAS using both anharmonic and harmonic methods has been detailed elsewhere (Zhang et al. 2024). Vibrationally-resolved C1s XAS spectra of  $\text{CN}^+/\text{CN}/\text{CN}^-$  were simulated using the wavepacket method based on multiconfigurational PECs with our XspecTime package (Hua & Wei 2023; Zhang et al. 2024). The program reads PECs of the initial and final electronic states, performs Morse fitting and computes the spectrum at 201 discrete points across C-N distances from 0.7 to 2.5 Å. The wavepacket was propagated for a duration of  $6 \times 10^6$  a.u. with a time step of 1.0 a.u. A HWHM lifetime of 0.05 eV for the C1s core hole was applied.

For comparison, we also simulated the vibrationally-resolved C1s XAS spectra based on the BLYP-DFT electronic structure under the harmonic oscillator (HO) approximation. Geometrical optimizations and vibrational frequency calculations were conducted both at the ground and the lowest C1s excited states using GAMESS-US (Schmidt et al. 1993; Gordon & Schmidt 2005). Subsequent Franck-Condon factor (FCFs) were simulated by using the modified (Hua et al. 2020) DynaVib package (Tian et al. 2012), which was interfaced with GAMESS-US to read the DFT results, including optimized structures, vibrational frequencies, normal modes, and integrals for both electronic states. Lorentzian broadening was adopted with a HWHM of 0.05 eV.

#### 2.5. *Valence-shell ionization potentials (IPs)*

With the equilibrium distances from multiconfigurational PECs at hand, we also computed the valence-shell vertical ( $V$ ) and adiabatic ( $A$ ) ionization potentials for  $\text{CN}^-$  and  $\text{CN}$ . These concepts are crucial for understanding molecular stability and electronic transitions. Studying  $\text{CN}^-$  and  $\text{CN}$  together facilitates a comparison of the ionization of the first and second electrons from  $\text{CN}^-$ . For example, for the ionization process  $\text{CN} \rightarrow \text{CN}^+ + e^-$ , vertical and adiabatic IPs are defined as potential energy differences between  $\text{CN}$  ( $E_{\text{CN}}$ ) and  $\text{CN}^+$  ( $E_{\text{CN}^+}$ ):

$$V = E_{\text{CN}^+}(R_{e,\text{CN}}) - E_{\text{CN}}(R_{e,\text{CN}}), \quad (2)$$

$$A = E_{\text{CN}^+}(R_{e,\text{CN}^+}) - E_{\text{CN}}(R_{e,\text{CN}}), \quad (3)$$

where  $R_{e,\text{CN}}$  and  $R_{e,\text{CN}^+}$  represent the equilibrium distances.

### 3. RESULTS AND DISCUSSION

#### 3.1. *Ground-state electronic structures*

Figure 1 illustrates the simulated BLYP energy level diagrams for  $\text{CO}^+$ ,  $\text{CN}^+$ ,  $\text{CN}$ , and  $\text{CN}^-$  in their optimized ground-state geometries. Each system exhibits distinct HOMO-LUMO gaps, where HOMO and LUMO refer to the highest occupied and the lowest unoccupied molecular orbitals, respectively. For the two open-shell systems,  $\text{CO}^+$  has  $\alpha$  and  $\beta$  gaps of 8.9 and 3.3 eV, respectively [Fig. 1(a)]. In contrast, its isoelectronic counterpart,  $\text{CN}$ , shows  $\alpha$  and  $\beta$  gaps of 8.0 and 1.5 eV, respectively [Fig. 1(c)]. For the two closed-shell systems,  $\text{CN}^+$  exhibits an exceptionally small gap of less than 0.1 eV [Fig. 1(b)], whereas  $\text{CN}^-$  displays a gap of 5.9 eV [Fig. 1(d)].

Despite these energy differences, orbital features across various species (and different spins of the same

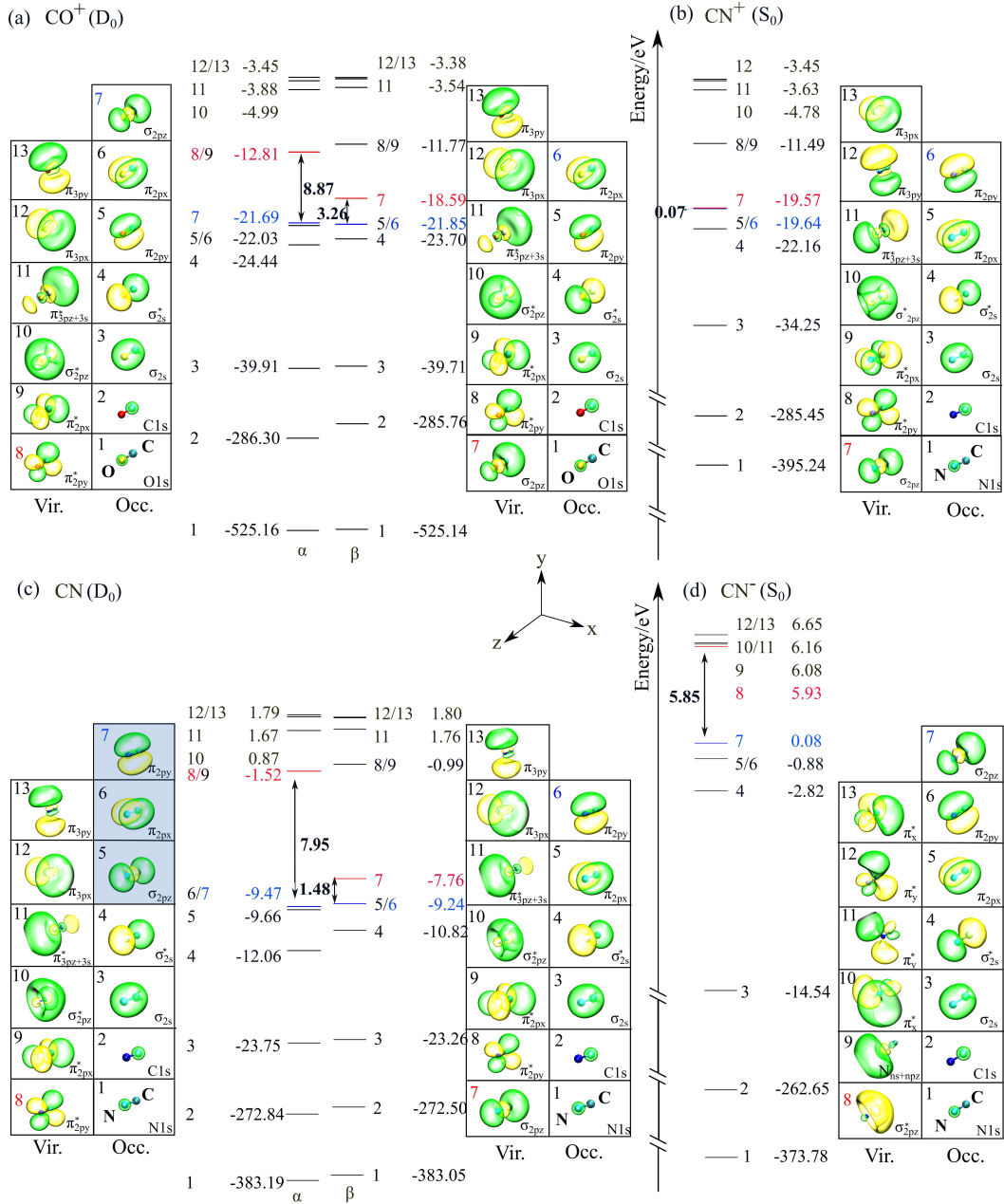


**Figure 1.** Energy level diagram of (a)  $\text{CO}^+$ , (b)  $\text{CN}^+$ , (c)  $\text{CN}$ , and (d)  $\text{CN}^-$  in their ground electronic states computed by DFT with the BLYP functional. In panels (a,c), spin-unrestricted DFT was used for  $\text{CO}^+$  and  $\text{CN}$ . Occupied and low-lying virtual MOs are shown in separate columns and interpreted by their major components. Shaded area in  $\text{CN}$   $\alpha$  occupied orbitals is to show a different order in MOs 5-7 ( $\sigma_{2pz}$ ,  $\pi_{2px}/\pi_{2py}$ ) as compared to others ( $\pi_{2px}/\pi_{2py}$ ,  $\sigma_{2pz}$ ). Degenerate orbitals are indicated by “/”. HOMO (blue) – LUMO (red) gap of each spin is indicated by arrows. All energies are in eV.

species) exhibit remarkable similarities. This holds for the occupied MOs of  $\text{CN}^-$  and both the occupied and unoccupied MOs of the other three systems. Specifically, in Fig. 1(a), MOs 1-10 for both  $\alpha$  and  $\beta$  spins of  $\text{CO}^+$  are characterized as follows:  $1s$ ,  $1s^*$ ,  $\pi_{2py}/\pi_{2px}$ ,  $\sigma_{2pz}$ ,  $\pi_{2py}^*/\pi_{2px}^*$ , and  $\sigma_{2pz}^*$ . (Note that delocalized  $\sigma_{1s}$  and  $\sigma_{1s}^*$  are absent here as we localized the  $1s$  orbitals, and “/” describes degenerate orbitals.) The  $\alpha$  and  $\beta$  orbitals of the same index are nearly identi-

cal. Figures 1 (b,c) show that orbitals of  $\text{CN}^+$  and  $\beta$  orbitals of  $\text{CN}$  have similar features and orders to those of  $\text{CO}^+$ . In contrast, the  $\alpha$  orbitals of  $\text{CN}$  present a different sequence for MOs 5-7 ( $\sigma_{2pz}$ ,  $\pi_{2py}/\pi_{2px}$ ), differing from the order observed in the orbitals of  $\text{CO}^+$ ,  $\text{CN}^+$ , and the  $\beta$  orbitals of  $\text{CN}$  ( $\pi_{2py}/\pi_{2px}$ ,  $\sigma_{2pz}$ ). Figure 1(d) illustrates that the occupied orbitals (MOs 1-7) of  $\text{CN}^-$  closely resemble those of  $\text{CO}^+$ ,  $\text{CN}^+$ , and the  $\beta$  orbitals of  $\text{CN}$ . However, the unoccupied orbitals are

more diffuse and mixed, showing significant differences from others and complicating their major MO feature interpretations. In summary,  $\text{CN}^-$  has notably different unoccupied orbitals compared to the other diatomic systems due to the presence of an extra electron.

### 3.2. XAS spectra

Figure 2 presents C1s XAS spectra of the four diatomic systems at their DFT-optimized ground-state geometries, simulated using DFT, RASSCF, and RASPT2 methods. Detailed positions and assignments for major peaks, labeled as  $i$  and  $ii$ , are provided in Table 1. For  $\text{CO}^+$ , theoretical predictions by all methods show strong agreement with each other and with the experiment (Couto et al. 2020), supporting the accuracy of our simulations. This also validates the accuracy of our predictions for the three C-N systems. The spectra of  $\text{CN}^+$  and CN show similar profiles to  $\text{CO}^+$ , except with redshifts of about 1.2 and 1.8 eV, respectively. In contrast, the  $\text{CN}^-$  spectrum is distinctly different from the other three, reflecting unique features in the unoccupied region, consistent with the ground electronic state.

Major peaks were interpreted using natural transition orbitals (NTOs) (Martin 2003; Malmqvist & Veryazov 2012), focusing on RASSCF [Fig. 2 (b)] and RASPT2 [Fig. 2 (d)] methods as examples. The weak peak  $i$  and strong peak  $ii$  for  $\text{CO}^+$ ,  $\text{CN}^+$ , and CN corresponds to  $\text{C1s} \rightarrow \sigma^*$  and  $\text{C1s} \rightarrow \pi^*$  transitions, respectively. This aligns with the unoccupied-level electronic structure in the ground state, where the  $\sigma_{2pz}$  orbital (MO 7; only the  $\beta$  spin for  $\text{CO}^+$  and CN) has lower energy than  $\pi_{2px}^*$  and  $\pi_{2py}^*$  (MOs 8-9), indicating relatively weak electronic relaxation due to the introduced core hole.

The  $\text{CN}^-$  spectrum, however, has different assignments. The lowest peak  $i$ , predicted at 286.11–286.69 eV, corresponds to  $\text{C1s} \rightarrow \pi^*$  transitions, including transitions to two degenerate  $\pi^*$  orbitals. In the higher energy region (ca. 298.10–298.82 eV), a broad peak arises from multiple  $\text{C1s} \rightarrow \text{C}np$  transitions, each with mixed components (see also Fig. A2 for a more localized view with a larger isovalue). The anion demonstrates the largest core hole effect due to significant differences in the electronic structures of the ground and core-excited states. DFT also reveals substantial differences compared to the three multiconfigurational simulations, highlighting the necessity of explicit static correlation. Consistency among the three multiconfigurational spectra indicates a weak influence of dynamical correlations.

### 3.3. Core-hole induced changes in bond lengths and vibrational frequencies

**Table 1.** Energies and assignments for major peaks (defined in Fig. 2) in the C1s XAS spectra of  $\text{CO}^+$ , CO,  $\text{CN}^+$ , CN, and  $\text{CN}^-$ , simulated using different methods and software at their ground-state equilibrium geometry. Peak energies here have been calibrated by adding a method-specific *ad hoc* shift  $\delta$  (see values in Fig. 2), obtained by aligning peak  $i$  of  $\text{CO}^+$  to the corresponding experiment (Couto et al. 2020). All energies are in eV, and  $\Delta$  denotes difference between peaks  $ii$  and  $i$ .

Cmpd.	Method	Peak $i$	Peak $ii$	$\Delta$
$\text{CO}^+$	BLYP-FCH	282.06	287.46	5.40
	RASSCF (MOLPRO)	282.06	289.90	7.84
	RASSCF (MOLCAS)	283.06	290.11	7.05
	RASPT2 (MOLCAS)	282.06	289.88	7.82
	Expt.	282.06	289.88	7.82
	Assignment	$\text{C1s} \rightarrow \sigma^*$	$\text{C1s} \rightarrow \pi^*$	
$\text{CN}^+$	BLYP-FCH	281.01	286.11	5.10
	RASSCF (MOLPRO)	282.22	289.50	7.28
	RASSCF (MOLCAS)	282.24	289.61	7.37
	RASPT2 (MOLCAS)	282.46	289.72	7.26
	Assignment	$\text{C1s} \rightarrow \sigma^*$	$\text{C1s} \rightarrow \pi^*$	
CN	BLYP	280.50	286.85	6.35
	RASSCF (MOLPRO)	279.76	288.78	9.02
	RASSCF (MOLCAS)	279.71	287.98	8.27
	RASPT2 (MOLCAS)	279.99	287.92	7.93
	Assignment	$\text{C1s} \rightarrow \sigma^*$	$\text{C1s} \rightarrow \pi^*$	
$\text{CN}^-$	BLYP-FCH	286.11	298.65	12.54
	RASSCF (MOLPRO)	286.69	298.36	11.67
	RASSCF (MOLCAS)	286.68	298.82	12.14
	RASPT2 (MOLCAS)	286.12	298.10	11.98
	Assignment	$\text{C1s} \rightarrow \pi^*$	$\text{C1s} \rightarrow p\text{Ryd}$	

Table A1 presents simulated bond lengths for each system in both the optimized ground state ( $l'$ ) and the lowest C1s core-excited state ( $l$ ), along with their difference ( $\Delta l \equiv l - l'$ ), as predicted by BLYP-DFT. It also includes the vibrational frequencies for the initial ( $\omega'$ ) and final ( $\omega$ ) states, with the corresponding change ( $\Delta\omega \equiv \omega - \omega'$ ). The changes in C-N bond lengths induced by C1s excitation for  $\text{CN}^+$ , CN, and  $\text{CN}^-$  are -5.6, -6.8, and -6.1 pm, respectively, indicating similar magnitudes of shortening across all three species. It is noted that this is quite system-dependent, as in  $\text{CO}^+$  and CO, the changes induced by the C1s core hole are -3.7 and +2.5 pm, respectively (Zhang et al. 2024).

The ground-state vibrational frequencies range narrowly from 2015.1 to 2070.9  $\text{cm}^{-1}$  (55.8  $\text{cm}^{-1}$  span), whereas excited-state frequencies increase and vary more widely from 2343.5 to 2467.6  $\text{cm}^{-1}$  (124.1  $\text{cm}^{-1}$  span), underscoring the strong influence of the core hole. The vibrational frequency changes show mild increases:

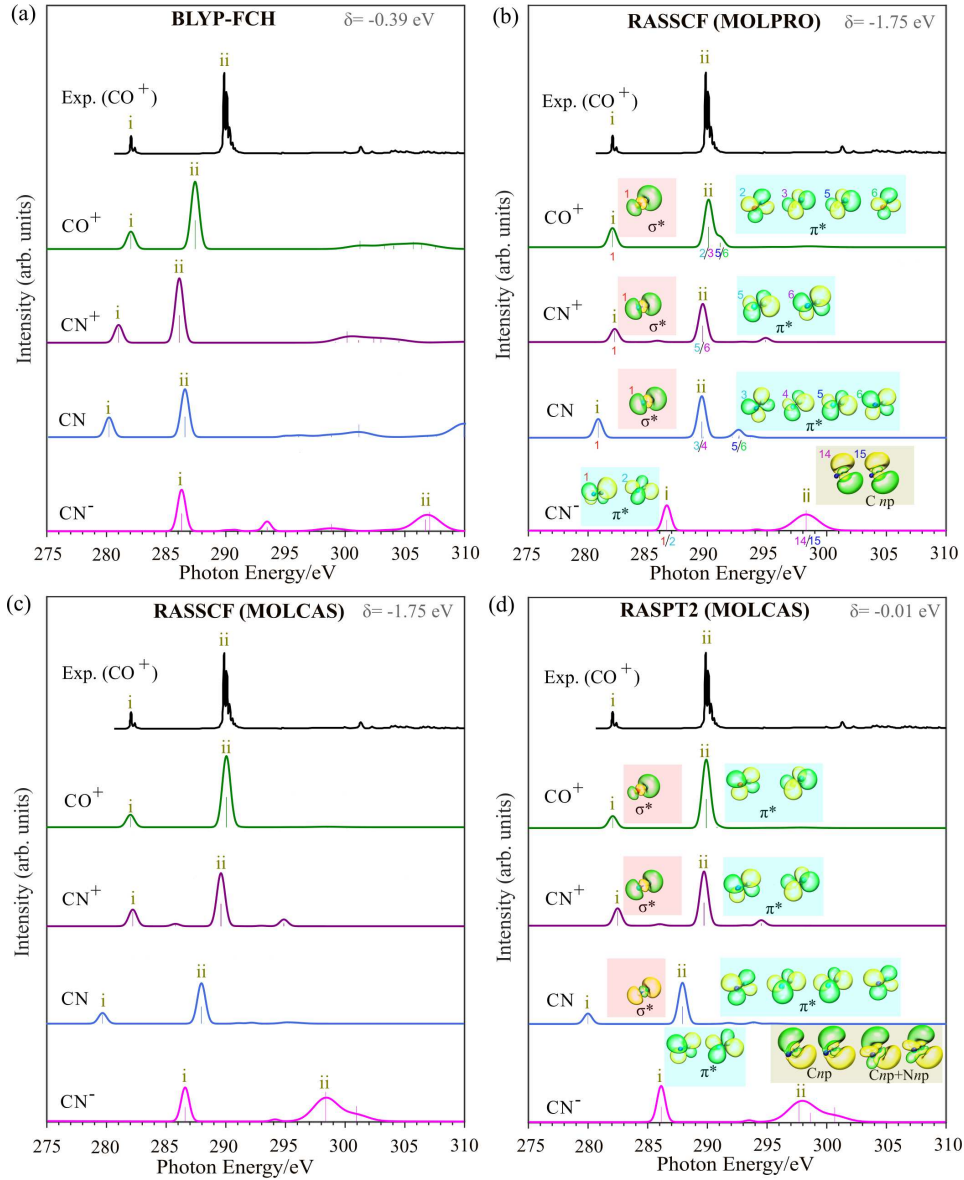


**Figure 2.** Simulated C1s XAS spectra for CO, CO<sup>+</sup>, CN, CN<sup>-</sup>, and CN<sup>+</sup> at their ground-state geometries, using different theoretical methods and software as indicated. For each method, the theoretical spectrum for CO<sup>+</sup> was shifted by  $\delta$  to align with experimental data (Couto et al. 2020), which was then applied to all other systems. In panels (b) and (d), major peaks are interpreted by NTOs alongside (note for degeneracy), with their major characteristics assigned and distinguished by three differently colored backgrounds.

CN<sup>+</sup> at 328.4 cm<sup>-1</sup>, CN at 377.8 cm<sup>-1</sup>, and CN<sup>-</sup> at 425.9 cm<sup>-1</sup>. The similar magnitudes parallel with the observed bond length shortening. Similar absolute shifts of several hundred wavenumbers due to C/N/O 1s core holes have been reported in other diatomic systems (Zhang et al. 2024).

### 3.4. Potential energy curves

Figure 3 illustrates PECs for the ground and the lowest C1s excited states of CN<sup>+</sup>, CN, and CN<sup>-</sup>, simulated using various electronic structure methods. All PECs are well-fitted to Morse potentials, with the resulting pa-

rameters detailed in Table A2. Within each method, the ground state curves decrease in the order of CN<sup>+</sup>, CN, and CN<sup>-</sup>, with CN<sup>+</sup> distinctly higher than the other two. In the core-excited state, CN<sup>+</sup> retains the highest energy, but the order of the CN and CN<sup>-</sup> curves is reversed. This shift arises from the core hole effect, which is significant due to the small energy separation between CN and CN<sup>+</sup> in the ground state, altering their relative energies.

The three multiconfigurational methods yield similar PECs, validating our predictions. In either the ground

or excited state, the predicted equilibrium bond lengths for the three species and by all methods show consistent values. For example, RASPT2 simulations predicted ground-state equilibrium bond lengths for  $\text{CN}^+$ , CN, and  $\text{CN}^-$  of 1.188, 1.176, 1.180 Å, respectively (Table A2). These values also align well with the optimized bond lengths of 1.183 Å ( $\text{CN}^+$ ), 1.183 Å (CN), and 1.172 Å ( $\text{CN}^-$ ) obtained using harmonic oscillator approximations and BLYP-DFT (Table A1).

Bond length shortening is illustrated both in Fig. 3 (highlighting  $\text{CN}^-$ ) and Table A2. The reduction of 4–6 pm due to the core hole effect is consistent with the 6–7 pm observed with harmonic oscillator approximations (Table A1).

In the ground state, the fitted dissociation energies ( $D_e$ ) increase across the series:  $\text{CN}^+$  (6.3–6.4 eV), CN (8.1–8.2 eV), and  $\text{CN}^-$  (9.4–10.3 eV) as shown in Table A2. While in the excited state, dissociation energies change significantly:  $\text{CN}^+$  (0.27 eV), CN (0.33 eV), and  $\text{CN}^-$  (0.22–0.25 eV), with CN now exhibiting the largest dissociation energy. These results highlight the strong influence of the core hole effect.

### 3.5. Valence-shell ionic potentials

Table A3 presents the simulated adiabatic and vertical IPs obtained from multiconfigurational calculations. In the ground state, the close agreement of two IP values indicates minimal structural rearrangement upon ionization. The RASPT2-predicted IPs for the  $\text{CN}^- \rightarrow \text{CN}$  and  $\text{CN} \rightarrow \text{CN}^+$  transitions are 3.6 and 13.7 eV, respectively. This highlights that ionizing a second valence electron from  $\text{CN}^-$  is significantly more challenging than the first. This observation aligns with chemical intuition: the extra electron in the anion is more loosely bound, while the outer electron in the neutral molecule experiences a larger effective nuclear charge, making it more tightly bound. RASSCF results are consistent but slightly underestimate the IPs, yielding values of 1.7–2.2 eV and 12.6–12.7 eV, reflecting the influence of dynamic correlation.

In Table A3, we also include corresponding simulated IPs for the lowest C1s excited state. This describes the shake-off process observed in XAS spectra, where the primary core excitation leads to the ionization of outer electrons. At the RASPT2 level, the computed vertical (adiabatic) IPs are -1.6 (-1.7) eV and 16.2 (16.1) eV, respectively. Typically, IP is a positive value; the computed negative IP for  $\text{CN}^-$  suggests that the shake-off process is less likely, indicating a less stable final state. By contrast, the positive IP for CN suggests a higher probability for this process. Similar to the ground state, RASSCF yields values comparable to RASPT2.

### 3.6. Vibronic fine structures

Figure 4 presents simulated vibronic fine structures for the lowest C1s excited states of  $\text{CN}^+$ , CN, and  $\text{CN}^-$ , derived from DFT and multiconfigurational methods. For each system, the three multiconfigurational methods yield nearly equivalent spectral profiles, validating the computational accuracy and indicating a weak influence of dynamic electron correlation on vibronic coupling. The most significant difference in the predicted spectra of the three systems lies in the energy positions of the 0-0 peaks: 280.7, 279.6, and 285.8 eV for  $\text{CN}^+$ , CN, and  $\text{CN}^-$ , respectively. While the profiles appear generally similar, each is dominated by the 0-0 peak, followed by a weaker 0-1 peak. The intensity ratio of the 0-1 peak to the 0-0 peak, denoted as  $F_{01}/F_{00}$  (Hua et al. 2020), is approximately 0.55, 0.75, and 0.49, respectively. Additionally, the predicted energy difference between the 0-0 and 0-1 peaks is  $\sim 0.23$  eV for  $\text{CN}^-$  and  $\sim 0.30$  eV for  $\text{CN}^+$  and CN. In the region beyond, an even weaker 0-2 peak is still identifiable in CN, but less visible in  $\text{CN}^-$  or  $\text{CN}^+$ . The similarity in profiles results from the resemblance of PECs (Fig. 3). The dominance of the 0-0 peak suggests the relatively small displacement of the PECs, consistent with bond length changes of 4-6 pm (Fig. 3 and Table A2).

The DFT curves exhibit a rough resemblance to the corresponding multiconfigurational results, yet they contain significant discrepancies. The reduced accuracy of the DFT results primarily arises from the harmonic oscillator approximation used. A previous study (Zhang et al. 2024) highlighted the pronounced sensitivity of anharmonic effects and the diminished responsiveness of electronic structure methods across several diatomic systems.

## 4. CONCLUSION AND OUTLOOK

In summary, we have theoretically predicted accurate C1s XAS spectra for  $\text{CN}^+$ , CN, and  $\text{CN}^-$  through multiconfigurational and DFT simulations, providing valuable references for future X-ray spectroscopic studies in astronomy and chemical physics. Due to the lack of experimental data,  $\text{CO}^+$ , an isoelectronic species of CN, was used for calibration and validation with various electronic structure methods. The first electronic peak for  $\text{CO}^+$ ,  $\text{CN}^+$ , and CN is assigned to  $\text{C1s} \rightarrow \sigma^*$  transitions, while that for  $\text{CN}^-$  corresponds to a  $\text{C1s} \rightarrow \pi^*$  transition. Vibronic fine structures for the lowest C1s transition, well-separated from higher absorptions, were computed using RASSCF- and RASPT2-level anharmonic PECs via the quantum wavepacket method, yielding consistent results. The 0-0 absorption energies are distinctly different at 280.7, 279.6, and 285.8 eV for the three sys-



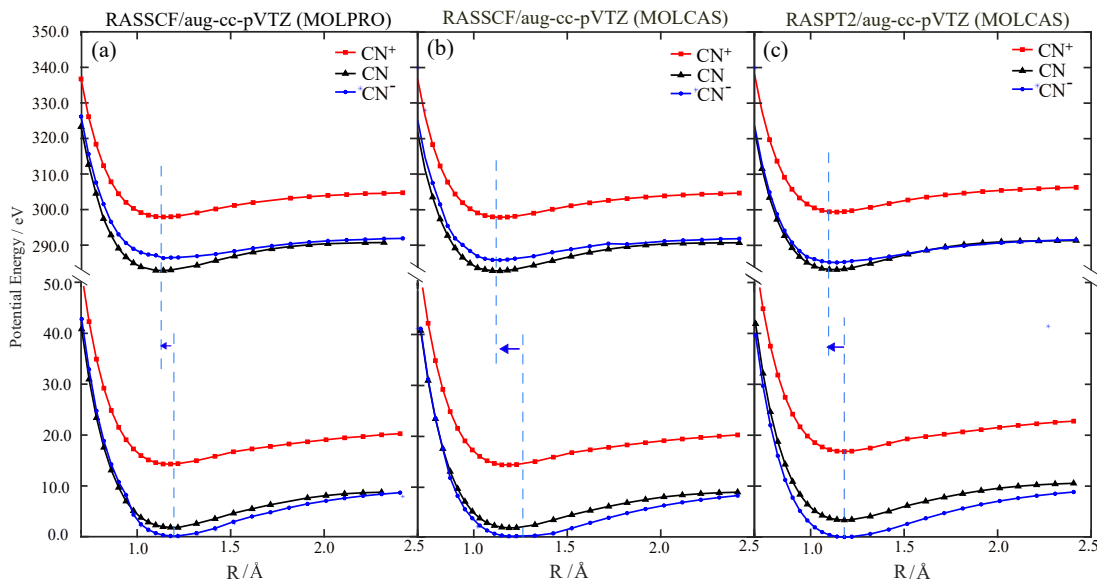


**Figure 3.** Simulated PECs for the ground (bottom) and the lowest C1s core-excited (top) states of  $\text{CN}^+$ ,  $\text{CN}$ , and  $\text{CN}^-$  using different methods (software used is indicated in parentheses) as indicated. In panel (d), (blue) dashed lines and arrow are to highlight the decrease in equilibrium positions, taking  $\text{CN}^-$  as an example.

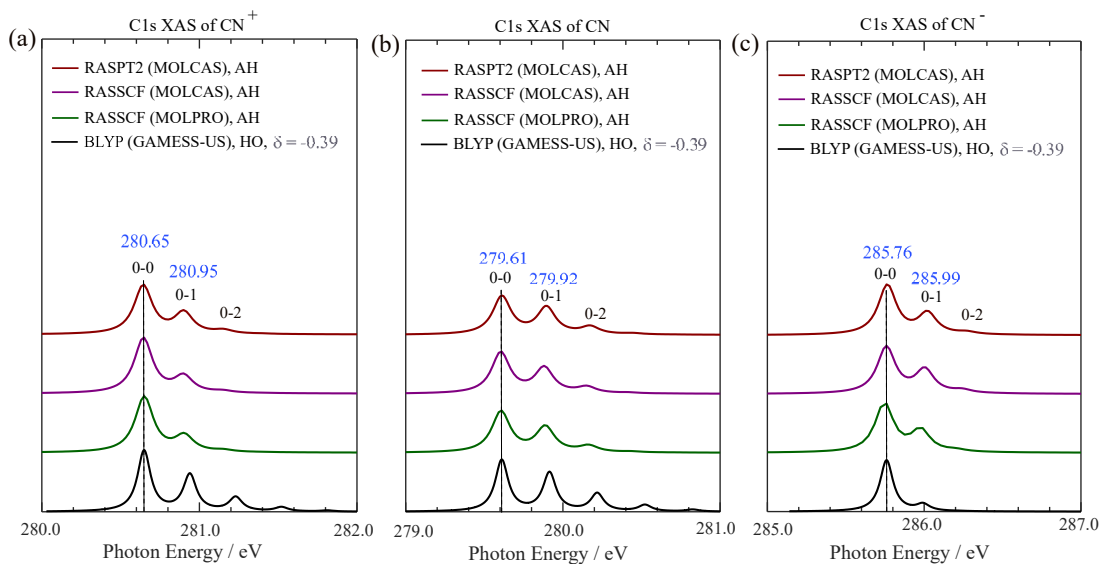


**Figure 4.** Vibrationally-resolved C1s XAS spectra for the lowest C1s excited state of (a)  $\text{CN}^+$ , (b)  $\text{CN}$ , and (c)  $\text{CN}^-$  simulated using various theoretical methods: BLYP-DFT method with the harmonic oscillator approximation and multiconfigurational methods combined with anharmonic PECs. To facilitate comparison with future experiments, an *ad hoc* shift of  $\delta = 0.39$  eV [derived from Fig. 2(a)] was applied to the BLYP spectrum. For clarity in fine structure comparisons, all other methods were aligned to the BLYP spectrum by adjusting the 0-0 peak.

tems. Although the vibronic profiles are similar, they differ in the intensity ratios of the 0-0 and 0-1 peaks. Spectra were assigned and correlated with ground-state electronic structures to investigate the core hole effect. PECs indicate a decrease of 4-6 pm in equilibrium bond lengths due to the C1s core hole for all species. Additionally, using the harmonic approximation with DFT, the C1s core hole leads to a bond length reduction of 6-7 pm and an increase in vibrational frequency of 300-400

$\text{cm}^{-1}$ . The resulting spectra closely match the vibronic fine structures from anharmonic calculations, underscoring the influence of anharmonicity. These findings enhance our understanding of the electronic structure, X-ray spectra, and vibronic coupling effects, illustrating the impact of charge state. Our group is also working on high-resolution X-ray emission and photoelectron spectra of molecules, aiming to establish a comprehen-

sive theoretical library that may aid X-ray astronomical studies of interstellar and circumstellar molecules.

#### ACKNOWLEDGMENTS

Financial support from the National Natural Science Foundation of China (Grant No. 12274229) is greatly acknowledged. Thanks to Prof. Jicai Liu for providing the Molpro software for part of the calculations.

#### APPENDIX

#### SUPPLEMENTARY MATERIALS

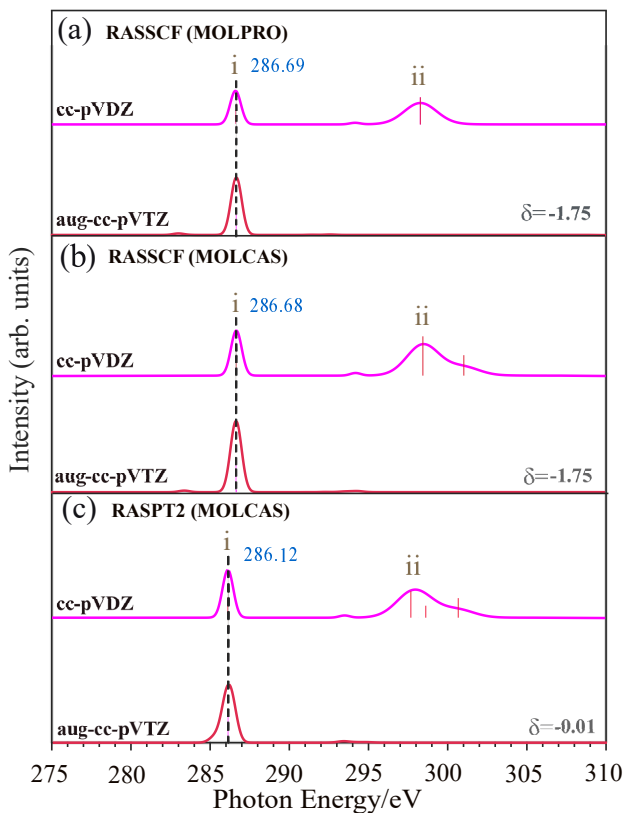


**Figure A1.** C1s X-ray absorption spectra of  $\text{CN}^-$  calculated using (a-b) RASSCF (with Molpro and openMolcas) and (c) RASPT2 methods with two different basis sets (cc-pVDZ and aug-cc-pVTZ), averaging over 30 electronic states. The aug-cc-pVTZ results were shifted by  $\delta = -1.75, -1.75,$  and  $-0.01$  eV (derived from  $\text{CO}^+$  calculations with the same basis set, see Fig. 2 (b)-(d) and the main text). Due to the limited number of states, only one major peak is observed at 286.69, 286.68, and 286.12 eV. Increasing the number of states met with the technical problem of convergence error. Thus, to capture a broader energy range, the cc-pVDZ spectrum was computed and calibrated to the aug-cc-pVTZ results by aligning the first peak.

**Table A1.** Comparison of simulated vibrational frequencies  $\omega$  (in  $\text{cm}^{-1}$ ) and optimized bond lengths (in  $\text{\AA}$ ) for ground state ( $\omega', l'$ ) and the lowest C1s excited state ( $\omega, l$ ) for  $\text{CN}^+, \text{CN},$  and  $\text{CN}^-$  calculated by DFT with the BLYP functional.  $\Delta\omega = \omega - \omega'$  and  $\Delta l = l - l'$  represent the frequency and bond length changes, respectively.

Cmpd.	$\omega'$	$\omega$	$\Delta\omega$	$l'$	$l$	$\Delta l$
$\text{CN}^+$	2015.1	2343.5	+328.4	1.183	1.127	-0.056
CN	2070.9	2448.7	+377.8	1.182	1.114	-0.068
$\text{CN}^-$	2041.7	2467.6	+425.9	1.172	1.111	-0.061

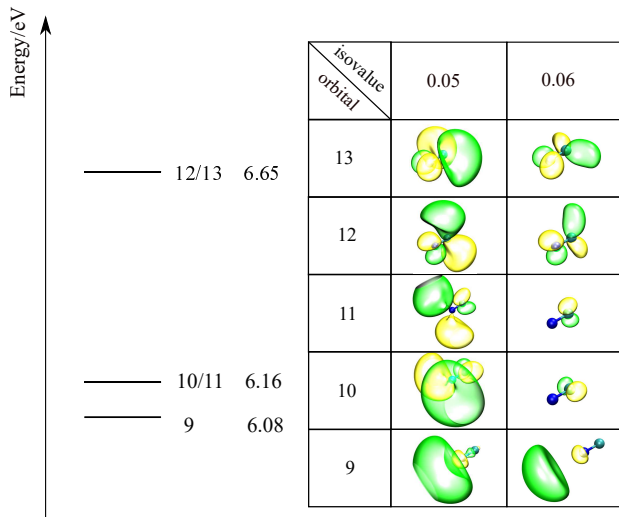


**Figure A2.** Enlarged view of Fig. 1(a) illustrating part of the BLYP-generated energy level diagram and selected molecular orbitals (MOs 9-13) of  $\text{CN}^-$ . An isovalue of 0.05 was used in the main text (left), while a larger isovalue of 0.06 was applied for comparison to obtain a more localized view (right).

**Table A2.** Fitted Morse (Morse 1929) parameters [see  $T_e$ ,  $D_e$ ,  $\alpha$ , and  $R_e$  in Eq (1)] for the potential energy curves of  $\text{CN}^+$ ,  $\text{CN}$ , and  $\text{CN}^-$ , obtained using various electronic structure methods (software used is indicated in parentheses). Superscripts 0 and 1 label the ground and the lowest C1s excited state, respectively.

Cmpd.	Method	Ground state				Lowest C1s excited state				$\Delta R_e$ ( $\text{\AA}$ )
		$T_e^0$ (eV)	$D_e^0$ (eV)	$\alpha^0$ (a.u.)	$R_e^0$ ( $\text{\AA}$ )	$T_e^1$ (eV)	$D_e^1$ (eV)	$\alpha^1$ (a.u.)	$R_e^1$ ( $\text{\AA}$ )	
$\text{CN}^+$	RASSCF (MOLPRO)	0.054	6.343	1.359	1.184	283.543	0.266	1.419	1.146	-0.038
	RASSCF (MOLCAS)	0.054	6.367	1.353	1.184	283.815	0.266	1.423	1.146	-0.038
	RASPT2 (MOLCAS)	0.082	6.367	1.345	1.188	282.454	0.268	1.434	1.141	-0.047
$\text{CN}$	RASSCF (MOLPRO)	0.136	8.191	1.280	1.181	281.366	0.332	1.409	1.128	-0.053
	RASSCF (MOLCAS)	0.054	8.055	1.280	1.183	281.366	0.326	1.394	1.129	-0.054
	RASPT2 (MOLCAS)	0.082	8.218	1.288	1.176	280.005	0.332	1.418	1.146	-0.056
$\text{CN}^-$	RASSCF (MOLPRO)	0.082	10.286	1.140	1.218	286.264	0.216	1.441	1.171	-0.047
	RASSCF (MOLCAS)	-0.435	9.415	1.195	1.203	285.992	0.237	1.456	1.154	-0.049
	RASPT2 (MOLCAS)	-0.136	10.123	1.209	1.180	284.903	0.250	1.481	1.136	-0.044

**Table A3.** Adiabatic ( $A^0$  and  $A^1$ ) and vertical ( $V^0$  and  $V^1$ ) ionization potentials (in eV) for two valence electron ionization processes: (1)  $\text{CN}^- \rightarrow \text{CN}$  and (2)  $\text{CN} \rightarrow \text{CN}^+$ , calculated using various electronic structure methods (software indicated in parentheses). Superscripts 0 and 1 denote the ground and the lowest C1s excited states, respectively. Negative values (highlighted in parentheses) indicate non-physical shake-off processes; see text for details.

No.	Method	Ground state		C1s excited state	
		$V^0$	$A^0$	$V^1$	$A^1$
1	RASSCF (MOLPRO)	1.807	1.734	(-3.286)	(-3.378)
	RASSCF (MOLCAS)	2.186	2.166	(-2.966)	(-2.990)
	RASPT2 (MOLCAS)	3.629	3.629	(-1.646)	(-1.655)
2	RASSCF (MOLPRO)	12.600	12.598	15.086	15.076
	RASSCF (MOLCAS)	12.653	12.653	15.034	15.025
	RASPT2 (MOLCAS)	13.719	13.715	16.164	16.146

## REFERENCES

- Agúndez, M., Marcelino, N., & Cernicharo, J. 2018, *ApJL*, 861, L22
- Agúndez, M., Cernicharo, J., Guélin, M., et al. 2010, *A&A*, 517, L2, doi: [10.1051/0004-6361/201015186](https://doi.org/10.1051/0004-6361/201015186)
- Amano, T. 2008, *JChPh*, 129, 244305, doi: [10.1063/1.3043739](https://doi.org/10.1063/1.3043739)
- Anderson, J., & Ziurys, L. 2014, *ApJL*, 795, L1
- Aquilante, F., Autschbach, J., Baiardi, A., et al. 2020, *JChPh*, 152, 214117, doi: [10.1063/5.0004835](https://doi.org/10.1063/5.0004835)
- Arnaud, K., Smith, R., & Siemiginowska, A. 2011, *Handbook of X-ray Astronomy* (Cambridge University Press)
- Bagus, P. S. 1965, *Phys. Rev.*, 139, A619, doi: [10.1103/PhysRev.139.A619](https://doi.org/10.1103/PhysRev.139.A619)
- Bagus, P. S., Sousa, C., & Illas, F. 2016, *JChPh*, 145, 144303, doi: [10.1063/1.4964320](https://doi.org/10.1063/1.4964320)
- Bakker, E. J., Waters, L., Lamers, H. J., Trams, N. R., & Van der Wolf, F. L. 1995, *A&A*
- Bambi, C., & Jiang, J. 2023, *High-Resolution X-ray Spectroscopy: Instrumentation, Data Analysis, and Science* (Springer Nature)
- Becke, A. D. 1988, *PhRvA*, 38, 3098, doi: [10.1103/PhysRevA.38.3098](https://doi.org/10.1103/PhysRevA.38.3098)
- Beckman, J. E. 2021, in *Multimessenger Astronomy* (Springer), 145–175
- Boger, G. I., & Sternberg, A. 2005, *ApJ*, 632, 302, doi: [10.1086/432864](https://doi.org/10.1086/432864)
- Brooke, J. S. A., Ram, R. S., Western, C. M., et al. 2014, *ApJS*, 210, 23, doi: [10.1088/0067-0049/210/2/23](https://doi.org/10.1088/0067-0049/210/2/23)
- Carniato, S., Bizau, J.-M., Cubaynes, D., et al. 2020, *Atoms*, 8, 67, doi: [10.3390/atoms8040067](https://doi.org/10.3390/atoms8040067)
- Couto, R. C., Kjellsson, L., Ågren, H., et al. 2020, *Phys. Chem. Chem. Phys.*, 22, 16215
- Dalgarno, A., & McCray, R. A. 1973, *ApJ*, 181, 95, doi: [10.1086/152032](https://doi.org/10.1086/152032)
- Delcey, M. G., Pedersen, T. B., Aquilante, F., & Lindh, R. 2015, *JChPh*, 143, 044110, doi: [10.1063/1.4927228](https://doi.org/10.1063/1.4927228)
- Du, X., Wang, S.-Y., Wei, M., et al. 2022, *Phys. Chem. Chem. Phys.*, 24, 8196, doi: [10.1039/D2CP00069E](https://doi.org/10.1039/D2CP00069E)
- Dunning, Jr., T. H. 1989, *JChPh*, 90, 1007, doi: [10.1063/1.456153](https://doi.org/10.1063/1.456153)
- Ehara, M., Nakatsuji, H., Matsumoto, M., et al. 2006, *JChPh*, 124
- Ezoe, Y., Ohashi, T., & Mitsuda, K. 2021, *Rev. Mod. Plasma Phys.*, 5, 1, doi: [10.1007/s41614-021-00052-2](https://doi.org/10.1007/s41614-021-00052-2)
- Fdez. Galván, I., Vacher, M., Alavi, A., et al. 2019, *J. Chem. Theory Comput.*, 15, 5925, doi: [10.1021/acs.jctc.9b00532](https://doi.org/10.1021/acs.jctc.9b00532)
- Finley, J., Malmqvist, P.-Å., Roos, B. O., & Serrano-Andrés, L. 1998, *Chem. Phys. Lett.*, 288, 299, doi: [10.1016/S0009-2614\(98\)00252-8](https://doi.org/10.1016/S0009-2614(98)00252-8)
- Gandhi, P. 2024, *Philos. Trans. R. Soc. A*, 382, 20230080, doi: [10.1098/rsta.2023.0080](https://doi.org/10.1098/rsta.2023.0080)
- Giacconi, R. 2003, *Rev. Mod. Phys.*, 75, 995
- Giacconi, R., Gursky, H., Paolini, F. R., & Rossi, B. B. 1962, *PhRvL*, 9, 439, doi: [10.1103/PhysRevLett.9.439](https://doi.org/10.1103/PhysRevLett.9.439)
- Gordon, M. S., & Schmidt, M. W. 2005, in *TACC* (Elsevier), 1167–1189
- Gottlieb, C. A., Brünken, S., McCarthy, M. C., & Thaddeus, P. 2007, *JChPh*, 126, 191101, doi: [10.1063/1.2737442](https://doi.org/10.1063/1.2737442)
- Granovsky, A. A. 2011, *JChPh*, 134, 214113, doi: [10.1063/1.3596699](https://doi.org/10.1063/1.3596699)
- Guélin, M., Muller, S., Cernicharo, J., et al. 2000, *A&A*, 363, L9
- Guélin, M., Muller, S., Cernicharo, J., McCarthy, M., & Thaddeus, P. 2004, *A&A*, 426, L49
- Hua, W. 2024, *Comput. Phys. Commun.*, 296, 109016, doi: [10.1016/j.cpc.2023.109016](https://doi.org/10.1016/j.cpc.2023.109016)
- Hua, W., Bennett, K., Zhang, Y., Luo, Y., & Mukamel, S. 2016a, *Chem. Sci.*, 7, 5922
- Hua, W., Luo, Y., & Mukamel, S. 2019a, *Multi-Configurational methods for ultrafast NOnlinear X-ray spectra (MCNOX), version 1.0*, [http://jszy.njust.edu.cn/lxy/hwj\\_en/list.psp](http://jszy.njust.edu.cn/lxy/hwj_en/list.psp)
- Hua, W., Mukamel, S., & Luo, Y. 2019b, *J. Phys. Chem. Lett.*, 10, 7172
- Hua, W., Oesterling, S., Biggs, J. D., et al. 2016b, *Struct. Dyn.*, 3, 023601
- Hua, W., Tian, G., & Luo, Y. 2020, *Phys. Chem. Chem. Phys.*, 22, 20014, doi: [10.1039/D0CP02970J](https://doi.org/10.1039/D0CP02970J)
- Hua, W., & Wei, M. 2023, *XSpecTime, version 0.9*
- Kaastra, J., Paerels, F., Durret, F., Schindler, S., & Richter, P. 2008, *SSRv*, 134, 155
- Kahn, S. M. 1999, *PhyS*, 1999, 23, doi: [10.1238/Physica.Topical.080a00023](https://doi.org/10.1238/Physica.Topical.080a00023)
- Kendall, R. A., Dunning, Jr., T. H., & Harrison, R. J. 1992, *JChPh*, 96, 6796, doi: [10.1063/1.462569](https://doi.org/10.1063/1.462569)
- Kutzelnigg, W., Fleischer, U., & Schindler, M. 1990, in *Deuterium and Shift Calculation, Vol. 23* (Berlin, Heidelberg: Springer Berlin Heidelberg), 165–262, doi: [10.1007/978-3-642-75932-1\\_3](https://doi.org/10.1007/978-3-642-75932-1_3)
- Lee, C., Yang, W., & Parr, R. G. 1988, *PhRvB*, 37, 785, doi: [10.1103/PhysRevB.37.785](https://doi.org/10.1103/PhysRevB.37.785)
- Li Manni, G., Fdez. Galván, I., Alavi, A., et al. 2023, *J. Chem. Theory Comput.*, 19, 6933, doi: [10.1021/acs.jctc.3c00182](https://doi.org/10.1021/acs.jctc.3c00182)

- Lindblad, R., Kjellsson, L., Couto, R., et al. 2020, *PhRvL*, 124, 203001, doi: [10.1103/PhysRevLett.124.203001](https://doi.org/10.1103/PhysRevLett.124.203001)
- Lindblad, R., Kjellsson, L., De Santis, E., et al. 2022, *PhRvA*, 106, 042814
- Longair, M. S. 1994, *J. High Energy Astrophys.*, 2, ch18
- Malmqvist, P. Å., Rendell, A., & Roos, B. O. 1990, *J. Phys. Chem.*, 94, 5477
- Malmqvist, P. Å., & Roos, B. O. 1989, *Chem. Phys. Lett.*, 155, 189
- Malmqvist, P. Å., Roos, B. O., & Schimmelpfennig, B. 2002, *Chem. Phys. Lett.*, 357, 230
- Malmqvist, P. Å., & Veryazov, V. 2012, *Mol. Phys.*, 110, 2455
- Mannings, V., Boss, A. P., & Russell, S. S. 2000, *Protostars and Planets IV* (University of Arizona Press)
- Martin, R. L. 2003, *JChPh*, 118, 4775
- McKellar, A. 1940, *Publ. Astron. Soc. Pac.*, 52, 187
- Morse, P. M. 1929, *Phys. Rev.*, 34, 57, doi: [10.1103/PhysRev.34.57](https://doi.org/10.1103/PhysRev.34.57)
- Oda, M. 1986, in *APRIM: September 30–October 5 1984, Kyoto, Japan Part 1*, Springer, 67–70
- Ohishi, M., McGonagle, D., Irvine, W. M., Yamamoto, S., & Saito, S. 1994, *ApJ*, 427, L51
- Püttner, R., Dominguez, I., Morgan, T., et al. 1999, *PhRvA*, 59, 3415
- Remijan, A. J., Hollis, J. M., Lovas, F. J., Plusquellic, D. F., & Jewell, P. 2005, *ApJ*, 632, 333
- Sarre, P. J. 1980, *J. Chim. Phys.*, 77, 769, doi: [10.1051/jcp/1980770769](https://doi.org/10.1051/jcp/1980770769)
- Savage, B. D., & Sembach, K. R. 1996, *ARA&A*, 34, 279, doi: [10.1146/annurev.astro.34.1.279](https://doi.org/10.1146/annurev.astro.34.1.279)
- Schilke, P., Comito, C., & Thorwirth, S. 2003, *ApJ*, 582, L101
- Schippers, S., Hillenbrand, P.-M., Perry-Sassmannshausen, A., et al. 2023, *ChemPhysChem*, 24, e202300061
- Schmidt, M. W., Baldrige, K. K., Boatz, J. A., et al. 1993, *J. Comput. Chem.*, 14, 1347, doi: [10.1002/jcc.540141112](https://doi.org/10.1002/jcc.540141112)
- Smith, D. 1988, *Philos. Trans. Royal Soc. A*, 324, 257
- Snyder, L. E. 1992, *Symposium-IAU*, 150, 427, doi: [10.1017/S0074180900090598](https://doi.org/10.1017/S0074180900090598)
- Snyder, L. E., & Buhl, D. 1971, *ApJ*, 163, L47
- Stålring, J., Bernhardsson, A., & Lindh, R. 2001, *Mol. Phys.*, 99, 103, doi: [10.1080/002689700110005642](https://doi.org/10.1080/002689700110005642)
- Takahashi, O., & Pettersson, L. G. M. 2004, *JChPh*, 121, 10339, doi: [10.1063/1.1809610](https://doi.org/10.1063/1.1809610)
- Tian, G., Duan, S., Hua, W., & Luo, Y. 2012, *DynaVib*, version 1.0
- Triguero, L., Pettersson, L. G. M., & Ågren, H. 1998, *PhRvB*, 58, 8097, doi: [10.1103/PhysRevB.58.8097](https://doi.org/10.1103/PhysRevB.58.8097)
- Triguero, L., Plashkevych, O., Pettersson, L., & Ågren, H. 1999, *J. Electron. Spectrosc. Relat. Phenom.*, 104, 195, doi: [10.1016/S0368-2048\(99\)00008-0](https://doi.org/10.1016/S0368-2048(99)00008-0)
- Trümper, J. 1993, *Science*, 260, 1769, doi: [10.1126/science.260.5115.1769](https://doi.org/10.1126/science.260.5115.1769)
- Werner, H.-J., Knowles, P. J., Knizia, G., Manby, F. R., & Schütz, M. 2012, *Wiley Interdiscip. Rev.: Comput. Mol. Sci.*, 2, 242, doi: [10.1002/wcms.82](https://doi.org/10.1002/wcms.82)
- Wilkes, B. J., Tucker, W., Schartel, N., & Santos-Lleo, M. 2022, *Nature*, 606, 261
- Yin, Y., Shi, D., Sun, J., & Zhu, Z. 2018, *ApJS*, 235, 25, doi: [10.3847/1538-4365/aab26b](https://doi.org/10.3847/1538-4365/aab26b)
- Zack, L., Halfen, D., & Ziurys, L. 2011, *ApJL*, 733, L36
- Zhang, L., Wei, M., Ge, G., & Hua, W. 2024, *PhRvA*, 109, 032815, doi: [10.1103/PhysRevA.109.032815](https://doi.org/10.1103/PhysRevA.109.032815)
- Zhang, Y., Hua, W., Bennett, K., & Mukamel, S. 2016, *Top. Curr. Chem.*, 368, 273
- Ziurys, L. M. 2006, *Proc. Natl. Acad. Sci.*, 103, 12274